



1 **Three-Dimensional Stefan Equation for Thermokarst Lake and Talik**
2 **Geometry Characterization**

3 **Noriaki Ohara¹, Benjamin M. Jones², Andrew D. Parsekian^{3,1}, Kenneth M. Hinkel⁴, Katsu**
4 **Yamatani⁵, Mikhail Kanevskiy², Rodrigo C. Rangel³, Amy L. Breen⁶, and Helena**
5 **Bergstedt²**

6

7 ¹Department of Civil and Architectural Engineering, University of Wyoming, Laramie, WY,
8 82071, USA

9 ²Institute of Northern Engineering, University of Alaska Fairbanks, Fairbanks, Alaska, 99775,
10 USA

11 ³Department of Geology and Geophysics, University of Wyoming, Laramie, WY 82071, USA

12 ⁴Department of Geological and Mining Engineering and Sciences, Michigan Technological
13 University, Houghton, MI 49931, USA

14 ⁵Department of Urban Science, Meijo University, 4-102-9 Yataminami, Higashi, Nagoya 461-
15 8534, Japan

16 ⁶International Arctic Research Center, University of Alaska Fairbanks, Fairbanks, Alaska

17 Corresponding author: Noriaki Ohara (nohara1@uwyo.edu)

18



19 **Abstract**

20 Thermokarst lake dynamics, which plays an essential role in carbon release due to permafrost
21 thaw, is affected by various geomorphological processes. In this study, we derive a three-
22 dimensional (3D) Stefan equation to characterize talik geometry under a hypothetical
23 thermokarst lake in the continuous permafrost region. Using the Euler equation in the calculus
24 of variations, the lower bounds of the talik were determined as an extremum of the functional
25 describing the phase boundary area with a fixed total talik volume. We demonstrate that the
26 semi-ellipsoid geometry of the talik is optimal for minimizing the total permafrost thaw under
27 the lake for a given annual heat supply. The model predicting ellipsoidal talik geometry was
28 verified by talik thickness observations using transient electromagnetic (TEM) soundings in
29 Peatball Lake on the Arctic Coastal Plain (ACP) of Alaska. The lake width-depth ratio of the
30 elliptic talik can characterize the energy flux anisotropy in the permafrost although the lake
31 bathymetry cross section may not be elliptic due to the presence of near-surface ice-rich
32 permafrost. This theory suggests that talik development stabilizes thermokarst lakes by ground
33 subsidence due to permafrost thaw while wind-induced waves and currents are likely responsible
34 for the elongation and orientation of thermokarst lakes in certain regions such as the ACP of
35 northern Alaska.



36 **1. Introduction**

37 Thermokarst lakes are abundant in regions underlain by ice-rich permafrost including the Arctic
38 Coastal Plain (ACP) of northern Alaska, northwestern Canada and Siberia (Grosse et al., 2013).
39 These lakes are formed due to permafrost degradation and their basin evolution is fundamentally
40 different from lakes formed in temperate and tropical regions. Thermokarst lakes affect the
41 thermal regime of the surrounding permafrost, which affects the geomorphology and evolution
42 of the lake basin. If the lake bed has a mean annual temperature greater than 0°C, the sub-lake
43 permafrost will begin to thaw (Burn, 2002; Arp et al., 2016). This typically occurs in lakes
44 deeper than the maximum winter ice thickness, where the ice cover floats above an unfrozen
45 water body. In this case, unfrozen lake bed sediments persist and the thaw front continues to
46 penetrate deeper into the underlying permafrost. This creates a “talik”, or a perpetually unfrozen
47 zone confined by permafrost, beneath the lake depending on local anomalies in thermal,
48 hydrological, hydrogeological, or hydrochemical conditions (van Everdingen, 1998). In ice-rich
49 permafrost, the conversion of ice to water with thaw causes a volumetric reduction in the
50 unconsolidated material and the lake bed consequently subsides. The total depth of subsidence is
51 determined by the depth and distribution of excess-ice content in the permafrost. As the lake
52 expands by lateral thermomechanical erosion (thermal abrasion) of the banks, mineral and
53 organic sediments from retreating shores are delivered to the lake basin (Farquharson et al. 2016).
54 However, thaw-induced ground subsidence effectively deepens the basin, so volumetric capacity
55 can actually increase over time. Over decades and centuries, the talik increases in thickness and
56 lake bed subsidence continues as long as the thawing permafrost is ice-rich.

57 In certain ice-rich permafrost regions in the Arctic, there is a preferential orientation and elliptic
58 shape to the numerous thermokarst lakes that occur there (Black and Barksdale, 1949; Hinkel et



59 al., 2005; Grosse et al., 2013). On the ACP of northern Alaska, many elliptical thermokarst lakes
60 have a long axes oriented 10–20 degrees west from true north, which is nearly perpendicular to
61 the prevailing wind direction (Sellmann, 1975; Carter, 1981). Hinkel et al. (2005, 2012) also
62 showed significant correlation between lake orientation and summer wind direction by analyzing
63 the geometric shape metrics of the thermokarst lakes and drained thermokarst lake basins
64 (DTLB) on the ACP of Alaska. It has been proposed that winds at the lake surface cause currents
65 and generate a two-cell circulation pattern which triggers thermomechanical bank erosion,
66 resulting in asymmetrical elliptical orientation (Livingstone, 1954; Rex, 1961; Carson and
67 Hussey, 1962; Mackay, 1992; Arp et al., 2011). The sublittoral shelves and bars typically found
68 in the deeper thermokarst lakes may also be formed by wind-driven currents and waves, and
69 warmer water temperatures (Carson and Hussey, 1962). The axis-oriented sublittoral shelves
70 make the orientation appear more pronounced in larger basins. Other processes also influence the
71 orientation of thermokarst lakes such as historical drained lake geometry, ground ice distribution,
72 and dune ridge orientation by aeolian sand transport (Carter, 1981).

73 Several numerical models have been proposed and applied that describe permafrost thaw for the
74 purpose of analyzing water and carbon cycles (e.g. Kessler et al., 2012). However, Schuur et al.
75 (2015) stress the need to better represent talik formation and geometries to more effectively
76 parameterize numerical models. Painter et al. (2016) demonstrated a coupled surface/subsurface
77 permafrost thermal hydrology model at the ice-wedge polygon scale. Kessler et al. (2012)
78 simulated carbon mobilization over 10,000 years on two neighboring thaw lakes located on
79 organic-rich Yedoma permafrost terrains in the northern Seward Peninsula, Alaska using a 3D
80 numerical thermal model. They demonstrated the effectiveness of model simulations for methane
81 emission from thermokarst lakes. Ling and Zhang (2003b) provided a numerical parametrization



82 of lake talik development, and showed that shallow thermokarst lakes are a significant heat
83 source affecting permafrost and talik geometries. Rowland et al. (2011) advanced the technique
84 by including parameter of advective heat transport on talik evolution. West and Plug (2008) and
85 Plug and West (2009) characterized the lake bathymetry including the effects of lake ice and
86 littoral shelves. These thermal models use long-term mean lake temperature as the Dirichlet
87 boundary condition and a uniform annual mean temperature profile as the initial condition.
88 Analytical and numerical models can provide dynamic solutions for the heat transfer equation
89 under quasi-steady state climate conditions. However, the existing models require prescribed
90 lake shapes (circle or ellipse) to obtain information on talik depths as opposed to modeling the
91 likely influence of talik evolution on lake shape – this work, in part, attempts to address this
92 shortcoming.

93 Direct drilling measurements of taliks below thermokarst lakes are difficult to obtain and only
94 exist in a few rare case studies (Brewer, 1958; Johnston and Brown, 1966; Roy-Leveilee and
95 Burn, 2017; Heslop et al., 2015). Geophysical methods can be used (e.g. Schwamborn et al.,
96 2000; Parsekian et al., 2019; Creighton et al., 2018; Sullivan et al., 2021; O’Neill et al., 2020);
97 however, it is time consuming and laborious to produce 3D subsurface images at the large scale
98 of lakes found in permafrost lowland regions. Since field measurements (coring, geophysics,
99 etc.) are spatiotemporally limited, numerical and analytical modelling is used to gain critical
100 insights into talik evolution. Mackay (1962) obtained the analytical vertical temperature profiles
101 below the water at the center of a circular lake by analytically solving the heat transfer equation.
102 Burn (2002) subsequently extended the solution for an elongated lake. This analytical model has
103 been used for lake process characterization because the quasi-steady state model was able to
104 reasonably quantify the talik thickness. For example, Hinkel and Arp (2015) applied the



105 temperature profile to 2100 lakes and found that larger, long-lived lakes (more than 66 ha) may
106 have taliks that penetrate through the permafrost (throughgoing talik) to the ground-water system
107 below in a region with permafrost that is up to 600 m thick.

108 These existing models require the prescribed lake shapes (circle or ellipse) to obtain the talik
109 depth; in fact, no existing studies explicitly provide an answer to the fundamental question: why
110 do thermokarst lakes tend to be elliptical and/or round? Also, in spite of several decades of
111 research focused on the orientation of thermokarst lakes in certain regions, no existing studies
112 explicitly explain why thermokarst lakes in some regions orient perpendicular to the prevailing
113 wind direction. The objective of this work is to implement a novel mathematical framework that
114 concurrently describes both the oriented nature of the thermokarst lakes and the talik depth
115 below the lakes. Previous models have calculated the talik development due to heat flow, though
116 most use some simplifying assumptions to reduce dimensionality. Separately, researchers have
117 hypothesized about elliptical lake morphology by invoking winds, currents, and erosion. Here,
118 we couple both the talik evolution and lake shape questions together in a single mathematical
119 model. Additionally, we intend to use this theory to demonstrate that the thermal gradient could
120 exert control on the depth/width ratio of the talik. In other words, the proposed theory aims to
121 isolate the most important process – sub-lake permafrost thaw and subsidence - from other
122 effects such as wind-wave erosion, thaw slumping, sediment redistribution and incoming
123 radiation imbalance, using thermally optimized lake geometry.



124 2. Theory

125 2.1 Basin integrated energy equation

126 Heat energy collected by a waterbody is used for phase boundary expansion as well as heat
127 conduction into the adjacent permafrost (e.g. French, 1996). From the energy balance equation
128 around the phase boundary, the energy for permafrost thaw is expressed as the subtraction of
129 heat conduction from the input energy at the phase boundary (Carslaw and Jaeger, 1959; Patel,
130 1968; Lunardini, 1981). Therefore, the energy conservation equation at the phase boundary can
131 be expressed as,

$$132 \quad q_f = q_{in} - q_c, \quad (1)$$

133 where q_f is heat for fusion or thawing (W/m^2); q_{in} is heat input at the phase boundary (W/m^2);
134 and q_c is heat conduction to the permafrost (W/m^2). These heat fluxes can be evaluated by the
135 following formulas:

$$136 \quad q_f = \phi v \rho L, \quad (2)$$

$$137 \quad q_{in} = q_{surf} - k_L \frac{dT}{dn}, \quad \text{and} \quad (3)$$

$$138 \quad q_c = -k_p \frac{dT}{dn}. \quad (4)$$

139 where ϕ is volumetric water content; v is thaw rate or advancement of talik boundary (m/s); ρ is
140 density of water (kg/m^3); L is latent heat for fusion (liquid-solid) of water (J kg^{-1}); q_{surf} is
141 additional heat input from ground surface around the lake shore (W/m^2); k_L is thermal
142 conductivity of unfrozen soil or lake water; and k_p is thermal conductivity of frozen soil
143 (permafrost); T is temperature ($^{\circ}\text{C}$); and n is outward normal from the interface into the soil (m).



144 When heat input from the surface is consumed for phase change without any loss ($q_c = q_{surf} =$
145 0), the well-known Stefan equation can be obtained from Equations (1) through (4) under the
146 quasi-steady state approximation (Stefan, 1891; Kurylyk & Hayashi, 2016). This study also
147 adopts the quasi-steady state approximation for the talik shape characterization.
148 As the thawing process is direction-dependent, it is convenient to use vector notation (Figure 1).
149 That is,

$$150 \quad \mathbf{q}_f = \mathbf{q}_{in} - \mathbf{q}_c. \quad (5)$$

151 The letter in bold denotes a vector. The fusion heat flux vector corresponds to thaw direction,
152 which is affected by the other two heat fluxes. Figure 1 also illustrates the thermal profiles
153 around the thaw lake in warm and cold seasons. The horizontal near-surface heat conduction is
154 influenced by the seasonality of the surface heat budget while the vertical heat conduction under
155 the lake remains unidirectional throughout the years. Clearly, the presence of the thaw lake
156 considerably alters the heat environment of the permafrost while the temperature slope at the
157 bottom of the permafrost may be approximated by the geothermal gradient in regions with thick
158 continuous permafrost such as the ACP. This directionality in the heat environment around the
159 lake may cause anisotropic talik expansion. Here, the phase change heat vector is expressed as
160 proportional to the normal heat input q_{in} , as follows:

$$161 \quad \mathbf{q}_f = (q_{f,x}, q_{f,y}, q_{f,z}) = (\xi q_{in}, \eta q_{in}, \zeta q_{in}) = q_{in}(\xi, \eta, \zeta) \quad (6)$$

162 where q_{in} is the input heat normal to the phase boundary, ξ, η , and ζ are the fusion energy
163 fractions of the heat input normal to the phase boundary with respect to x, y, and z directions,
164 respectively. The depth of the phase boundary, $z = \varphi(x, y)$, may be expressed as an arbitrary 3D
165 surface as,



166
$$g(x, y, z) = \varphi(x, y) - z = 0. \quad (7)$$

167 Hence, the normal vector \mathbf{n} at any location on the phase boundary g can be written as follows:

168
$$\mathbf{n} = \frac{\nabla g}{|\nabla g|} = \frac{1}{|\nabla g|} (g_x, g_y, g_z) = \frac{1}{\sqrt{\varphi_x^2 + \varphi_y^2 + 1}} (\varphi_x, \varphi_y, -1) \quad (8)$$

169 where the subscript in this expression denotes partial derivative (e.g. $\varphi_x = \partial\varphi/\partial x$) and ∇ is a
 170 vector differential operator ($\partial/\partial x, \partial/\partial y, \partial/\partial z$). As such, the vector of the input heat to the
 171 phase boundary φ is

172
$$\mathbf{q}_{in} = |\mathbf{q}_{in}| \mathbf{n} = q_{in} \mathbf{n} = \frac{q_{in}}{\sqrt{\varphi_x^2 + \varphi_y^2 + 1}} (\varphi_x, \varphi_y, -1), \quad (9)$$

173 and the corresponding fusion heat vector is,

174
$$\mathbf{q}_f = \frac{q_{in}}{\sqrt{\varphi_x^2 + \varphi_y^2 + 1}} (\xi\varphi_x, \eta\varphi_y, -\zeta). \quad (10)$$

175 Next, the fusion heat magnitude can be evaluated using a Euclidian norm as,

176
$$|\mathbf{q}_f| = \frac{q_{in}}{\sqrt{\varphi_x^2 + \varphi_y^2 + 1}} \sqrt{\xi^2\varphi_x^2 + \eta^2\varphi_y^2 + \zeta^2} = \frac{\zeta q_{in}}{\sqrt{\varphi_x^2 + \varphi_y^2 + 1}} \sqrt{\alpha_x^2\varphi_x^2 + \alpha_y^2\varphi_y^2 + 1} \quad (11)$$

177 where

178
$$\alpha_x = \frac{\xi}{\zeta}, \quad \alpha_y = \frac{\eta}{\zeta}. \quad (12)$$

179 The parameters α_x and α_y describe the anisotropic thermal condition between horizontal and
 180 vertical directions. The parameters α_x and α_y are greater than one when the vertical temperature
 181 gradient is steeper than in horizontal direction. The total fusion energy over the lake can be
 182 computed by the area integral on the phase boundary Γ . That is,



$$\begin{aligned} 183 \quad \int_{\Gamma} |\mathbf{q}_f| d\Gamma &= \iint_B |\mathbf{q}_f| \sqrt{\varphi_x^2 + \varphi_y^2 + 1} dx dy \\ 184 \quad &= \zeta q_{in} \iint_B \sqrt{\alpha_x^2 \varphi_x^2 + \alpha_y^2 \varphi_y^2 + 1} dx dy. \end{aligned} \quad (13)$$

185 This expression indicates that the heat required for lake expansion is proportional to the weighted
186 phase boundary area.

187 **2.2 Optimum phase boundary shape as extremum**

188 The calculus of variation, often referred to as a functional analysis, is the mathematical technique
189 to find an extremum (minimum or maximum) of the system in terms of a function type instead of
190 a variable (e.g. Courant and Hilbert, 1954; Gelfand and Fomin, 1963). Here, we present the
191 thermally optimum function type $\varphi(x, y)$ of the phase boundary using this method. As presented
192 in the previous section, the heat consumption rate for talik expansion is represented by the
193 weighted phase boundary area while the time-integrated heat supply is equivalent to the thawed
194 permafrost volume. Assuming heat thaws the most susceptible region of the permafrost near the
195 heat source first, the shape of a talik may minimize the total permafrost thaw with a given
196 amount of incoming energy. Hence, this variational principle states that the optimum talik shape
197 should minimize the phase boundary area for the total talik expansion. The weighted phase
198 boundary area A and its volume V can be expressed as follows:

$$199 \quad \begin{cases} V[\varphi] = \iint_B \varphi dx dy \\ A[\varphi] = \iint_B \sqrt{\alpha_x^2 \varphi_x^2 + \alpha_y^2 \varphi_y^2 + 1} dx dy \end{cases} \quad (14)$$

200 The functional F is defined as

$$201 \quad F[\varphi] = \lambda V[\varphi] + A[\varphi] = \iint_B (\lambda \varphi + \sqrt{\alpha_x^2 \varphi_x^2 + \alpha_y^2 \varphi_y^2 + 1}) dx dy \quad (15)$$



202 where λ is a constant. Extremum of the functional F can be determined for $\lambda < 0$ because both
 203 V and A are monotonic functions. Let

$$204 \quad f(\varphi, \varphi_x, \varphi_y) = \lambda \varphi + \sqrt{\alpha_x^2 \varphi_x^2 + \alpha_y^2 \varphi_y^2 + 1}. \quad (16)$$

205 Equation (15) becomes,

$$206 \quad F[\varphi] = \lambda V[\varphi] + A[\varphi] = \iint_B f(\varphi, \varphi_x, \varphi_y) \, dx dy. \quad (17)$$

207 To find the extremal phase-boundary shape φ that minimizes the functional $F[\varphi]$, the Euler's
 208 Equation can be formulated as,

$$209 \quad \frac{\partial f(\varphi, \varphi_x, \varphi_y)}{\partial \varphi} - \frac{\partial}{\partial x} \left(\frac{\partial f(\varphi, \varphi_x, \varphi_y)}{\partial \varphi_x} \right) - \frac{\partial}{\partial y} \left(\frac{\partial f(\varphi, \varphi_x, \varphi_y)}{\partial \varphi_y} \right) = 0. \quad (18)$$

210 Substituting Equation (16) to (18) yields,

$$211 \quad \lambda - \frac{\partial}{\partial x} \left(\frac{\alpha_x^2 \varphi_x}{\sqrt{1 + \alpha_x^2 \varphi_x^2 + \alpha_y^2 \varphi_y^2}} \right) - \frac{\partial}{\partial y} \left(\frac{\alpha_y^2 \varphi_y}{\sqrt{1 + \alpha_x^2 \varphi_x^2 + \alpha_y^2 \varphi_y^2}} \right) = 0. \quad (19)$$

212 By analogy to two-dimensional application in Ohara and Yamatani (2019), an ellipsoid is one of
 213 the solutions of Equation (19), as follows:

$$214 \quad z = -\varphi = -\sqrt{\frac{4}{\lambda^2} - \frac{x^2}{\alpha_x^2} - \frac{y^2}{\alpha_y^2}} + d, \text{ or} \quad (20)$$

$$215 \quad \left(\frac{x}{\frac{2\alpha_x}{|\lambda|}} \right)^2 + \left(\frac{y}{\frac{2\alpha_y}{|\lambda|}} \right)^2 + \left(\frac{z-d}{\frac{2}{|\lambda|}} \right)^2 = 1. \quad (21)$$

216 Detailed alternative derivation using isoperimetric inequality is available in the Appendix A. The
 217 coefficients d and λ can be determined by further variational analysis explained in Appendix B.

218 As such, Equations (20) and (21) become



219
$$\varphi = \sqrt{D^2 - \frac{x^2}{\alpha_x^2} - \frac{y^2}{\alpha_y^2}}, \text{ and} \quad (22)$$

220
$$\left(\frac{x}{\alpha_x D}\right)^2 + \left(\frac{y}{\alpha_y D}\right)^2 + \left(\frac{z}{D}\right)^2 = 1, \text{ respectively.} \quad (23)$$

221 D is the talik center depth, α_x & α_y are the cross-sectional aspect ratios. Hence, the semi-
222 ellipsoidal geometry of the phase boundary (i.e., the boundary between the permafrost and talik)
223 was explicitly derived as a thermally optimum shape based on the variational principle using the
224 thermal quasi-steady state approximation; this is the 3D Stefan Equation for the talik beneath a
225 thermokarst lake.

226 **2.3 Thermokarst lake bathymetry and phase boundary geometry**

227 When top-down permafrost thaw dominates the process, the thermokarst lake bottom shape
228 $\psi(x, y)$ may be similar to the phase boundary shape, as illustrated in Figure 2. However, the
229 lake bathymetry can be related to the permafrost degradation rate defined as,

230
$$r_{deg} = \frac{D_{thaw}}{D_{frzn}} \sim 1 - \frac{\psi(x,y)}{\varphi(x,y)} \sim 1 - \frac{H}{D}, \quad (24)$$

231 where H and D denote the water depth and the talik thickness at the lake center, respectively.
232 D_{frzn} is the frozen soil thickness (m) and D_{thaw} is the corresponding thawed soil thickness depth
233 (m), which is strongly dependent on the excess ground ice content; excess ice is defined as the
234 volume of ice in the ground which exceeds the total pore (van Everdingen, 1998; Kanevskiy et
235 al., 2013). Therefore, thaw settlement is typically computed from wedge-ice volume content and
236 the thickness of the layer with excess ground ice. However, as the consolidation settlement
237 effect, which is a function of void ratio and effective stress, may not be separated, we use the
238 simple permafrost degradation rate (Equation 24) in this study.



239 If the permafrost degradation rate is uniform and constant throughout the basin (Panel A:
240 uniform permafrost in Figure 2), the lake bathymetry tends to be an ellipsoid shape. However, as
241 the ice-rich layer (ice wedges) is typically developed near the surface on the ACP (e.g.
242 Kanevskiy et al., 2013, 2016), the bathymetry may have a flatter bottom like a rectangular cross
243 section (Panel B: layered permafrost in Figure 2) because the ice-rich layer is characterized by
244 much higher thaw settlement than the ice-poor permafrost at depth. Therefore, proportionality
245 between talik thickness and lake water depth or uniform permafrost is unlikely reasonable
246 assumption due to the ice rich layer presence. Indeed, Hinkel et al. (2012) showed many flat-
247 bottomed lakes through the extensive bathymetry surveys across the ACP of Alaska using a
248 GPS-enabled sonar from a boat.

249 Additionally, as hydrology also affects the lake water level, the apparent lake bathymetry or lake
250 water depth, $h(x, y)$ must be adjusted by the water loss (or gain) per unit area. Therefore,

$$251 \quad h(x, y) = [1 - r_{sub}] \varphi(x, y) - H_{loss} , \quad (25)$$

252 where H_{loss} (m) is the elevation difference between the current water surface and original ground
253 surface before lake formation. At the lake center,

$$254 \quad H = [1 - r_{sub}] D - H_{loss} . \quad (26)$$

255 Thus, the thermokarst lake bathymetry is affected by the ice-rich layer thickness, interannual
256 water balance, lake age, and talik geometry.



257 **3. Case study**

258 **3.1 Study area**

259 Peatball Lake (70°42.40N, 153°55.50W; 3 m above sea level) on the ACP of Alaska was chosen
260 for the demonstrative model application in this study as it has been relatively well-documented.
261 Figure 3 shows the location of Peatball Lake as well as the subregions that will be presented later.
262 Peatball Lake, named for the abundant submerged peat balls on the lake bed, is a subcircular lake
263 on the Outer Coastal Plain of Alaska with a surface area of 1.18 km². Permafrost in this area is as
264 thick as 410 m (Jorgenson et al., 2007), and the average volumetric ground ice content is about
265 77% in the near surface to a depth of 4 m (Kanevskiy et al., 2011). A talik has formed under
266 Peatball Lake because the maximum water depth of 2.5 m exceeds the maximum winter ice
267 thickness of 1.5 to 2.0 m (Arp et al., 2015; Lenz et al., 2016). The talik depth was estimated as
268 91 m at the lake center based on noninvasive TEM measurements (Creighton et al., 2018).
269 However, the talik may not be present beneath the sublittoral shelves on the western shore from
270 the bathymetry (Lenz et al., 2016). Additionally, Lenz et al. (2016) reported that, based on
271 remote sensing imagery, Peatball lake has expanded laterally between 0.02 m/year and 1.36
272 m/year between 1955 and 2002.

273 **3.2 Geophysical survey of talik**

274 Geophysical field methods are effective for identifying and visualizing the frozen-unfrozen
275 interface, which is a key feature in permafrost dynamics (e.g. Pilon et al., 1985; Doolittle et al.,
276 1990; O'Neill et al., 2020; Rangel et al., 2021). For lake taliks in the continuous permafrost zone,
277 Schwamborn et al. (2002) analyzed the sedimentary history of Lake Nikolay in the western Lena
278 River Delta using seismic reflection and ground penetrating radar (GPR). Other geophysical



279 methods such as surface nuclear magnetic resonance (NMR) can be used to detect lake taliks
280 (Parsekian et al., 2019) and remnant taliks in drained lake basins (Rangel et al., 2021). At
281 Peatball Lake, Creighton et al. (2018) estimated the talik depth using transient electromagnetic
282 (TEM) surveys along transects perpendicular to lakeshores.

283 We applied the derived 3D Stefan equation to Peatball Lake based on the 27 talik thickness point
284 measurements across the lake (Figure 4), estimated using TEM soundings (Creighton et al.,
285 2018) during spring 2016 and 2017. Figure 4 shows the observed talik thicknesses by the TEM
286 sounding (dots) and the fitted theoretical talik thickness estimates (contour lines) superimposed
287 over the corresponding lake bathymetry measured by Lenz et al., 2016.

288 The geometric parameters of the semi-ellipsoid model such as the talik center depth (D), the
289 cross-sectional aspect ratios (α_x & α_y), lake orientation azimuth angle and the lake center
290 location were systematically determined by grid searching to minimize the root mean square
291 difference (RMSD) between the model and thaw front obtained from the TEM data. The
292 optimum parameters for the smallest RMSD (5.94 m) are shown in Figure 4. Unexpectedly, the
293 basin orientation angle was found to be 23 degrees east from true north, unlike the orientation of
294 other surrounding lakes in the region. Comparison between the extrapolated talik geometry and
295 the lake bathymetry (Lenz et al., 2016) suggests the possibility of coalescence of two basins in
296 the past; a relatively common occurrence on the ACP of Alaska. However, if we had more TEM
297 measurement points, particularly in the “possible talik sub-basin”, the fitted talik geometry could
298 be different as the model was only fitted for the 27 TEM soundings. Lake taliks tend to have a
299 semi-ellipsoidal shape, at least locally, as indicated by the very good fit of the elliptic model to
300 the TEM measured talik thicknesses (see Figure 4 with overall RMSD = 5.94 m). The idealized,



301 thermally optimum geometry model can be used to analyze lake formation history of the
302 irregular talik associated with multi-generation lakes such as Peatball Lake.

303 Additionally, the gaps between the shoreline and the modeled talik extent located along north
304 and east shores occur where lake expansion is occurring most rapidly (Lenz et al., 2016). It has
305 been reported that thaw lake banks continuously retreat through a combination of thermal and
306 mechanical processes, although there is significant variability in rate of bank retreat depending
307 on region (Hopkins, 1949; Hopkins et al., 1955; Tomirdiaro, 1982; Rampton, 1982; Burn and
308 Smith, 1990; Jones et al. 2011, Lenz et al., 2016). Cross-sectional numerical thermal models
309 demonstrated that the expansion rates are affected by the talik thickness (Plug and West, 2009)
310 and seasonal snow cover (Ling and Zhang, 2003a). The disagreement between the lake and talik
311 extents on the north and east shores of Peatball lake implies that rapid horizontal lake expansion
312 can locally dominate permafrost thaw and subsidence processes even in a lake with a talik.

313 Figure 5 compares the observed lakebed and talik profiles in Peatball Lake along the north-south
314 center line and along transects (b) –(c), respectively. Note that the TEM transects for the talik is
315 not a straight line (See figure 4); therefore, the fitted theoretical line shows irregularity. Figure
316 5A illustrates that the lakebed profile is characterized by flatter trapezoidal geometry compared
317 to the elliptic talik. In fact, there is a clear inflection in the linear regression line at a talik depth
318 of ~50 m in Figure 5B. From the slopes of the regression lines, the permafrost degradation rates
319 r_{deg} are computed as 97.3 % and 99.7 % for the shallow talik section (50 m or less) and the deep
320 section (50 m or more), respectively. This analysis suggests that the subsidence due to
321 permafrost thaw continues even after the shallow ice-rich part of the permafrost (about 4 meters,
322 Kanevskiy, 2011) is thawed while it has diminished around the depth of 50 meter under Peatball



323 lake. This case study demonstrates a link between lake bathymetry and talik thickness associated
324 with a layered permafrost structure and the wind erosion effect.

325 **3.3 Depth-width ratio and temperature gradient**

326 The analysis (Equations 22 & 23) suggests the proportional relationship between lake/talik
327 geometry and thaw energy. That is,

$$328 \quad a : b : D = \alpha_x : \alpha_y : 1 = \xi : \eta : \zeta = q_{f,x} : q_{f,y} : q_{f,z} \quad . \quad (27)$$

329 Combining Equations (27), (1) and (4), the depth-width (radius) ratio of the talik may be written
330 as follows:

$$331 \quad a : D = \left(q_{in,x} + k_p \frac{dT}{dr} \right) : \left(q_{in,z} + k_p \frac{dT}{dn} \right) \quad (28)$$

332 where r and n are the horizontal and vertical distances from the original permafrost surface
333 center, respectively, and a is the representative horizontal radius of the lake. This expression
334 states that the anisotropic top-down permafrost thaw is caused by anisotropy of the thermal
335 gradient for uniform incoming energy and uniform thermal properties of near surface
336 permafrost. For example, since the vertical thermal gradient is typically steeper than the
337 horizontal gradient during the critical summer months (Carson and Hussey, 1962; illustration in
338 Figure 1), the heat energy in the vertical direction is used more for heat conduction rather than
339 permafrost thawing. The vertical temperature gradient is always negative near the talik
340 boundary in the permafrost $\left(\frac{dT}{dn} < 0 \right)$ at the center of the lake while the inter-seasonal average
341 of the horizontal thermal gradient may be negligible $\left(\frac{dT}{dr} \approx 0 \right)$. Assuming the normal heat flux
342 to the phase boundary is uniform throughout the phase boundary surface $(q_{in,x} = q_{in,z} = q_{in})$,
343 Equation (28) can be simplified as follows:



344
$$\frac{D}{a} = 1 + \frac{k_p}{q_{in}} \frac{dT}{dn} \quad , \text{ or } \quad q_{in} = -\frac{ak_p}{a-D} \frac{dT}{dn} \quad . \quad (29)$$

345 This simple expression may be a useful tool to link the lake depth-width ratio, the lake average
346 heat flux q_{in} , and the vertical temperature gradient $\frac{dT}{dn}$ at the base of the talik. Since $\frac{dT}{dn} < 0$ in
347 the permafrost near the talik boundary, the D/a is always less than 1 (flatter than a semi-sphere).
348 However, the depth-width ratio of the talik depends on the vertical temperature slope near the
349 talik boundary, which is likely affected by talik age. For instance, Mackay's analytical model
350 (1962) suggests that the vertical temperature gradient below the lake center begins steeply at the
351 talik initiation, and then over time it approaches a lower slope at equilibrium. Therefore, the
352 formula in Equation (29) suggests that a younger talik should be flatter while an older talik
353 approaches a deeper semi-spheric shape ($D/a \rightarrow 1$).

354 Table 1 shows the estimated incoming heat flux with the key parameters using the proposed
355 formula (Equation (29)). Creighton et al. (2018) applied the CRYOGRID2 model (Westerman et
356 al., 2013) to Peatball Lake. The temperature slope at the talik bottom at the lake center was
357 estimated by the Mackay's analytical model assuming the lake age of 1400 years since the talik
358 initiation with the same model configuration Creighton et al. (2018) adopted. Creighton et al.
359 (2018) estimated the interannual mean heat flux q_{in} to be $0.070 \text{ (W/m}^2\text{)}$, which is very close to
360 our estimate. As this simplified formula is consistent with the well-configured modeling result,
361 the horizontal thermal gradient contribution to the vertical aspect ratio of the talik seems to be
362 very small in Peatball Lake.

363 Moreover, this relationship may be useful to incorporate the three-dimensional talik expansion
364 effect in a simple analysis without fully integrated permafrost thermal modeling. For example, if
365 the mean energy flux increases 10 percent from current climate conditions (e.g. shorter lake



366 freeze period), assuming all other properties are equal, the talik depth-width ratio D/a would shift
367 from 0.171 to 0.234 toward the new equilibrium state. Therefore, this analysis suggests that the
368 warmer climate may promote permafrost thaw in the vertical direction more than in the
369 horizontal direction. Hence, it is important to quantify the vertical thawing as well as the visible
370 lake horizontal expansion in order to evaluate the impact of the climate change on permafrost
371 thaw beneath thermokarst lakes.

372 **4. Discussion**

373 **4.1 Relationship between hypothetical models**

374 To illustrate the applicability of the thermal model presented here, the available hypothetical
375 models of thermokarst lake growth are compiled in Figure 6. This diagram focuses on the
376 physical processes after the lake initiation stage assuming the bio-ecological effects are
377 negligible.

378 Figure 6 illustrates the evolution of the talik in ice-rich permafrost over time, with driving
379 processes shown in the right panel. In Stage A, the mechanical processes of wave erosion and
380 thaw slumping along lake margins dominate lake expansion in summer, and shallow water favors
381 grounded lake ice in the winter. In time (Stage B), the lake deepens from thaw subsidence
382 beneath the older lake center. Winter ice may freeze to the lake bed, but heat loss is insufficient
383 to freeze the underlying thawed lake bed sediments. A shallow talik develops as thermal
384 processes work in tandem with mechanical processes, the latter now enhanced by more vigorous
385 lake circulation. By Stage C, the talik is well developed beneath the entire lake basin as ground
386 subsidence continues. Eventually (Stage D), the winter ice cover no longer extends to the lake
387 bed, but instead floats atop a residual pool of lake water, while milder vertical temperature



388 gradient beneath the lake deepens the talik as the lake matures. Thermomechanical erosion of
389 lake margins, especially if there are prominent banks in hilly terrain, promotes sedimentation on
390 near-shore shelves, and the underlying talik may begin refreezing. If the lake hasn't drained by
391 this point (Stage E), the talik beneath the lake center extends deeper into the permafrost although
392 subsidence may cease as the excess ice content diminishes with depth. Where many large, old
393 lakes exist, the permafrost may be riddled with deep taliks, and some may eventually penetrate to
394 the permafrost base to create a through-going talik.

395 Talik development is a natural processes governed by local conditions, but can be impacted by
396 direct and indirect human activities. Conditions that favor talik initiation and growth include:

- 397 • Deepening lake waters triggered by greater precipitation and/or reduced evaporation,
398 which promotes a floating ice regime
- 399 • Presence of ice-rich sediments (e.g., Yedoma) beneath lakes
- 400 • Warmer lake water induced by regional warming or by longer ice-free summers
- 401 • Thinner winter ice cover due to warmer winter temperatures and/or deeper snow

402 Conversely, talik growth cessation or contraction can occur when these same drivers are reversed,
403 if the lake partially or completely drains, or when the lake basin is filled with sediments. The
404 latter scenario is more likely in hilly terrain when the expanding lake erodes high banks and lake
405 currents redistribute sediments.



406 4.2 Thermal process and preferential expansion

407 4.2.1 Lake geometry and heat balance

408 The analytical expression of the lake geometry may be useful to analyze the horizontally oriented
409 lakes as well. From Equation (27) and (1), we have,

$$410 \quad a:b = q_{f,x}:q_{f,y} = (q_{in,x} - q_{c,x}):(q_{in,y} - q_{c,y}), \quad (30)$$

411 where a and b are the semi-major and -minor axes of the elongated lake, respectively. When
412 horizontal heat conduction into the tundra is negligible, ($q_{c,r} = k_p \frac{dT}{dr} \approx 0$), this equation can be
413 reduced to,

$$414 \quad a:b = q_{in,x}:q_{in,y}. \quad (31)$$

415 Hence, the aspect ratio of elliptic lakes can be explained by heat supply inequality if the lake
416 geomorphology process is dominated by thermal process. As expressed in Equation (3), there are
417 two different components in the incoming heat flux to the lake banks: surface energy flux and
418 heat conduction from the lake water body. Thus, the lake aspect ratio may be written as,

$$419 \quad a:b = \left(q_{suf,x} - k_L \frac{dT}{dx}\right): \left(q_{suf,y} - k_L \frac{dT}{dy}\right) \quad (32)$$

420 4.2.2 Incoming radiation imbalance effect

421 One of the incoming surface energy flux inequalities q_{suf} may be caused by shortwave radiation
422 along the lake shoreline. The daily potential solar irradiation on a sloping surface can be
423 computed by the trigonometric function (e.g. Equation B.11 in DeWalle and Rango, 2008). The
424 total daily radiation is a function of latitude and bank slope angle, which depends on the
425 permafrost degradation rate, the maturity of the talik, and ground ice distribution.



426 Figure 7 shows the computed mean daily potential solar irradiation on the sloping lakeshore (I'_q)
427 relative to a flat surface (I_q) during the summer period (June–August) at three different latitudes.
428 The shape of this diagram may correspond to the shape of a thermokarst lake as the enhanced
429 radiation results in more permafrost thaw. The difference in relative incoming radiation will
430 diminish as bank slope angle lessens. In general, the south facing slope along the northern shore
431 tends to receive more radiation than the north facing slope (e.g. Séjourné et al., 2015). This
432 tendency is more pronounced in lower latitude zones due to the higher mid-day sun angle.

433 It is interesting that at 65 and 60 degree latitude the north and south facing banks receive slightly
434 less radiation than east and west facing slopes, while an opposite result occurs at 70 degree
435 latitude (Figure 7). Therefore, the radiation imbalance may partially explain the north-south
436 elongation along the 70 degree latitude line and the west-east elongation of lower latitude (60–65
437 degrees) of lowland thermokarst lakes shown by Grosse et al. (2013, Figure 19). However,
438 because these small differences in incoming radiation imbalance alone are insufficient to result
439 in the distinctive lake elongation in the ACP, they likely introduce rather minor additional
440 complexities in lake spatial shape.

441 **4.3 Wind wave erosion and preferential expansion**

442 Wind wave erosion plays an important role in horizontal expansion of shallow lakes because
443 waves can undercut the vegetated bank (Hopkins, 1949). Wind wave asymptotically makes the
444 water bodies (e.g. lakes and bays) round by local net sediment flux even in low latitude regions
445 (e.g. Ashton et al., 2009). The effect of waves on shoreline morphology has been analyzed in the
446 coastal engineering field: for example, Silvester (1974) investigated the equilibrium shape of
447 bays under different wave conditions using laboratory wave experiments and found that the



448 stable beach in the bay adapted a half-heart or cardioid shape for a fixed wave direction in the
449 absence of sediment supply. Reeve et al. (2018) showed theoretically that the equilibrium
450 coastline shape can be expressed as a diffusion type equation through incorporating the wave
451 diffraction effect, which makes the wave crest line nearly parallel to the shore. However,
452 according to the shallow water wave theory, which is applicable for small fetch distances on
453 lakes in the ACP, water waves do not cause any sediment transport without current, although
454 wave motion is a key factor for the mobilization of the sediment (e.g. Carson and Hussey, 1962).

455 Wind-induced water circulation in a shallow, oval lake was perhaps first analyzed by
456 Livingstone (1954) who showed theoretically that the current around the lake ends may be
457 accelerated efficiently by wind-induced return rip currents. However, the lake water circulation
458 pattern assumed in his study (shown in the left side of Figure 8) was less common than the
459 pattern described by Carson and Hussey (1962), who observed reverse circulation patterns near
460 the lake ends, as shown in the right side of Figure 8. For convenience, we refer to two distinctive
461 current patterns: the Livingstone type and the Carson & Hussey (C&H) type. C&H type
462 circulation can indeed explain the commonly observed peat and sediment bars near the leeward
463 lake side shores. Carson and Hussey (1962) noted that sedimentation on the leeward lake side
464 can provide protection from mechanical wave erosion as well as insulation from permafrost thaw,
465 which result in lake elongation. They also observed that preferential bank erosion is typically
466 focused in zones oriented 50 degrees to wave approach. The return flow was found to
467 concentrate around the windward lake side, which accelerates the mechanical erosion and
468 sediment transport at the lake ends. However, the Livingstone type circulation might occur
469 depending on the local wind field as it can explain the sublittoral shelf formation on the
470 windward shore. In either case, the wind-induced current effect on lake elongation can be



471 supported by Livingstone's theory (1954) which should be valid for both circulation types. Thus,
472 the combination of wind wave mobilization and lake water circulation is the most accepted
473 hypothesis for lake elongation during the relatively young shallow lake expansion stage (Carson,
474 1968; Arp et al., 2011, Hinkel et al., 2012).

475 The shallow wave theory states that the sediment mobilization due to wind wave only occurs in
476 shallow water (wave height >4 % of water depth, e.g. Reeve et al., 2018). Therefore, the
477 contribution of the wind wave effect to lake elongation may be reduced as the lake deepens.

478 Figure 9 shows a plot of lake length:width ratios versus the percent of lakes with a bedfast ice
479 regime in seven study regions in Alaska determined with satellite-based synthetic aperture radar
480 imagery (Engram et al., 2018). The study regions represent differences in permafrost

481 characteristics and climate that appear to be reflected in this comparison of length:width ratio
482 and the percent of lakes in a region that freeze to their bed and thus likely do not have a sub-lake
483 talik. For example, lakes in the Teshekpuk Lake and Kuparuk study areas have a shape that is

484 nearly twice as long as it is wide. In both of these regions, more than 80% of the lakes freeze to
485 their bed and likely do not have a talik. This is contrast to lakes located near Umiat and on the
486 Seward Peninsula, that have primarily developed in Yedoma permafrost deposits. Lakes near

487 Umiat and on the Seward Peninsula tend to be more circular ($L:W = 1.3$ to 1.4) and more than
488 90% likely have a talik since they do not freeze to their bed in the winter. The differences
489 observed here relative to elongation of lakes and whether the region primarily has lakes that

490 freeze to their bed or not likely demonstrates a key aspect related to the role of wind-wave
491 erosion. In general, the shallower lakes common in coastal areas, such as Teshekpuk, Barrow,
492 and Kuparuk, are more elongated likely due to wind wave erosion. Whereas lakes in Umiat and

493 Inigok with a thicker ice-rich permafrost layer tends to rounder because of more rapid talik



494 development and more subsequent subsidence. This remote-sensing based evidence implies that
495 the wind effect seems to be limited by the lake thermal subsidence due to talik development
496 underneath while the lake with the bedfast ice may continue elongating by the wind erosion.

497 **4.4 Applicability of the 3D Stefan equation**

498 The limitations of the derived 3D Stefan Equation (Equation 22) are summarized in this section
499 along with Figure 6. Once a seasonal pond is formed on the permafrost, it primarily expands
500 horizontally by wind wave erosion and the thaw slump process (Carson & Hussey, 1962;
501 Livingstone, 1954; Rex, 1961; Hinkel et al., 2012, Grosse et al., 2013) because the active layer
502 beneath the pond likely freezes every year. On the flat ACP of Alaska, lake thaw slump tends to
503 be the result of topography (e.g. slope and aspect of the ground surface) while lake elongation is
504 likely caused by wind wave erosion. As described above, preferential bank thaw at the lake ends
505 can be explained by the insulation effect of the sediments carried by the water current (likely, the
506 C&H type circulation) because the sublittoral shelf may be initiated at this stage.

507 When seasonal thawing penetrates more deeply than the annual freezing depth, a talik may be
508 initiated, typically around the deepest point near the center of the lake (Lachenbruch et al. 1962).
509 Sellmann (1975) described this process, which is one of the mechanisms for shelf formation in a
510 thermokarst lake. For the horizontal expansion stage A in Figure 6, the proposed quasi-steady
511 state thermal model may not be appropriate because the lakeshore expansion imbalance occurs at
512 least minimally throughout the lake expansion process. However, the 3D Stefan equation may
513 be able to characterize the talik in the initiation stage B in Figure 6.

514 Once the talik is established, the 3D Stefan's thermal model proposed here suggests that the talik
515 may begin to influence lake geometry. Since sediment mobilization due to wind-driven waves



516 occurs in shallow water, lake elongation by waves may diminish as the lake deepens via ground
517 subsidence (Figure 9). Lake water effectively collects energy from the surface during summer
518 and the talik stores the excess heat throughout the winter. Arp et al. (2010, 2011) and Jefferies et
519 al. (1999) discussed the difference in heat conduction between a grounded ice lake and a floating
520 ice lake. Their observations are generally consistent with the proposed theory because a deeper
521 talik under a floating ice lake should have a greater heat capacity. Since lake elongation likely
522 occurs before talik formation, the horizontal lake characterization derived in this study may not
523 be fully applicable to the analysis of thaw lakes on the ACP. In fact, the disagreement of the
524 talik and lake extents in Peatball Lake application illustrates the multiple effects on the lake
525 bathymetry and orientation. Clearly, however, talik expansion and concurrent subsidence
526 stabilizes lake geometry and contributes to lake roundness.

527 The applicability of the proposed 3D Stefan equation must be limited for lakes with high
528 sediment influx and for lakes with through talik. The paired sublittoral shelves on both lake sides
529 are commonly found in the sand dune areas of the southern ACP. The talik shape is likely altered
530 by uneven sediment deposition that affects the temperature gradient normal to the phase
531 boundary as mentioned by several researchers (Mackay, 1992; Hunter et al., 1981; West and
532 Plug, 2008). The shelves created by sediment redistribution due to lake water circulation adds
533 complexity to the ellipsoidal talik shape described in this study. Finally, if the talik penetrates
534 through the permafrost and becomes a throughgoing talik (Hinkel and Arp, 2015), the proposed
535 thermal theory herein is no longer applicable for thermokarst lake and talik characterization.



536 **5. Conclusions**

537 The theory presented here addresses the origin of the thermokarst lake ellipticity on the ACP.

538 Elliptic lake geometry results from minimizing overall thawing energy consumption for a given
539 incoming energy load. This is particularly applicable for mature, deep thermokarst lakes with
540 well-developed taliks. Additionally, existing hypothetical models were reviewed to illuminate
541 the thermal effect on the thermokarst lake morphology.

542 The derived ellipsoid talik model integrates the atmospheric forcing (or incoming energy), the
543 vertical thermal gradient, the thermal diffusivity of the permafrost, and the talik geometry. Heat
544 flux by conduction into the permafrost depends on the heat gradient of the underlying permafrost
545 (Fourier's law). As the vertical temperature slope diminishes with talik maturation, the depth-
546 width ratio of the talik becomes larger creating a deeper talik; thus, much of incoming energy is
547 likely consumed for vertical rather than horizontal expansion. Conversely, during the early stages,
548 thermo-mechanical processes such as wind-driven wave erosion dominates horizontal expansion
549 and elongation of the lake. Consequently, this theory elucidates how talik expansion and
550 concurrent permafrost degradation stabilizes the shape of thermokarst lake to one that is more
551 round rather than elliptical.

552 The semi-ellipsoidal 3D Stefan equation is, to our knowledge, the first geometric model
553 explicitly derived only from the energy conservation equation at the phase boundary. The vector
554 form of the energy conservation equation (Equation 5) in a 3D anisotropic thermal field was
555 integrated at the phase boundary area under the isolated general-shaped lake to quantify the total
556 energy balance. It was shown that the total lake fusion energy or lake expansion rate is
557 equivalent to the weighted phase boundary area. The optimum talik shape function was



558 determined by the variational principle as an extremum of the functional that minimizes the total
559 thawing energy consumption. Thus, the resultant semi-ellipsoid equation (Equation 22) can be
560 considered the 3D Stefan equation because it describes the optimum geometry of phase boundary.

561 The derived semi-ellipsoid function was applied to Peatball Lake, ACP of Alaska, where the
562 talik was extensively surveyed using TEM soundings. The pure geometric fitting exercise met
563 the 27 measured TEM data point well with RMSD of 5.94 m, although the talik orientation
564 disagreed with orientation of Peatball Lake and other surrounding lakes. This may be induced by
565 the irregularity due to the rapid and uneven horizontal lake expansion, or possibly by basin
566 coalescence. Comparing the observed talik thickness to the observed lake bathymetry indicated
567 two distinctive permafrost degradation scenarios: significant subsidence by near-surface ice-rich
568 layer thaw and minor contribution of subsidence due to ice-poor permafrost thaw at depth.

569 Consequently, lake water depth is affected by uneven subsidence of thawing permafrost, the
570 interannual water balance; the spatial lake shape irregularity was determined during earlier stage
571 of development. Therefore, careful consideration is required for the analysis of the relationship
572 between lake bathymetry and talik thickness. Nevertheless, this theoretical technique can be
573 used as guidance to partition various effects such as talik development and thaw subsidence,
574 wind wave erosion, lake ice thickness, surficial geology type, and sediment transport by lake
575 water current.

576 **Appendix A: Alternative derivation using isoperimetric inequality**

577 Alternative derivation may provide the thermally optimum talik shape minimizing the phase
578 boundary area A with a fixed talik volume V . Equation (14) establishes talik volume and phase
579 boundary area under the thermokarst lake by a general function of the phase boundary φ . The



580 horizontal coordinate system may be transformed by $(u, v) = \left(\frac{x}{\alpha_x}, \frac{y}{\alpha_y}\right)$. Then, the phase
 581 boundary can be expressed as a scaled function,

$$582 \quad \hat{\varphi}(u, v) = \varphi(x, y) = \varphi(\alpha_x u, \alpha_y v), \quad (u, v) \in \hat{B}. \quad (\text{A1})$$

583 According to,

$$584 \quad \begin{cases} \frac{du}{dx} = \frac{1}{\alpha_x}, \\ \frac{dv}{dy} = \frac{1}{\alpha_y}, \\ \frac{\partial}{\partial u} \hat{\varphi}(u, v) = \frac{\partial}{\partial u} \varphi(\alpha_x u, \alpha_y v) = \alpha_x \varphi_x, \\ \frac{\partial}{\partial v} \hat{\varphi}(u, v) = \frac{\partial}{\partial v} \varphi(\alpha_x u, \alpha_y v) = \alpha_y \varphi_y \end{cases} \quad (\text{A2})$$

585 the talik volume and the phase boundary area can be written as,

$$586 \quad \begin{cases} V[\varphi] = \alpha_x \alpha_y \iint_{\hat{B}} \hat{\varphi} \, dudv \\ A[\varphi] = \alpha_x \alpha_y \iint_{\hat{B}} \sqrt{\hat{\varphi}_u^2 + \hat{\varphi}_v^2 + 1} \, dudv = \alpha_x \alpha_y \int_{\hat{S}} d\hat{S} \end{cases}, \quad (\text{A3})$$

587 where \hat{B} denotes the extent of $\hat{\varphi}(u, v)$ on the uv plane, and \hat{S} is the surface on $z = \hat{\varphi}(u, v)$ as,

$$588 \quad \hat{S} = \{ (u, v, z) \in \mathbb{R}^3 \mid (u, v) \in \hat{B}, z = \hat{\varphi}(u, v) \}. \quad (\text{A4})$$

589 The horizontal scaling transform makes it a symmetric closed surface on $z = 0$,

$$590 \quad S^* = \{ (u, v, z) \in \mathbb{R}^3 \mid (u, v) \in \hat{B}, z = \pm \hat{\varphi}(u, v) \}. \quad (\text{A5})$$

591 It is known that volume U enclosed by the ovaloid surface S^* and its surface area satisfy the
 592 isoperimetric inequality for an ovaloid surface, which can be written as,

$$593 \quad \left(\int_{S^*} dS^* \right)^3 \geq 36\pi U^2. \quad (\text{A6})$$



594 As the volume and the surface area of the convex closed surface S^* can be expressed as

$$595 \quad U = 2 \left| \iint_{\hat{B}} \hat{\varphi} \, dudv \right| = \frac{2}{\alpha_x \alpha_y} |V[\varphi]|, \text{ and} \quad (\text{A7})$$

$$596 \quad \int_{S^*} dS^* = 2 \int_{\hat{S}} d\hat{S} = \frac{2}{\alpha_x \alpha_y} A[\varphi], \text{ respectively,} \quad (\text{A8})$$

597 we have,

$$598 \quad \left(\frac{2}{\alpha_x \alpha_y} A[\varphi] \right)^3 \geq 36\pi \left(\frac{2}{\alpha_x \alpha_y} V[\varphi] \right)^2, \text{ or}$$

$$599 \quad A[\varphi] \geq \sqrt[3]{18\pi \alpha_x \alpha_y (V[\varphi])^2}. \quad (\text{A9})$$

600 The equality in Equation (A9) holds only if the surface S^* is a sphere, which maximizes the
 601 volume. Let the radius of this sphere,

$$602 \quad D = \sqrt[3]{\frac{3}{4\pi} V} = \sqrt[3]{\frac{3|A[\varphi]|}{2\pi \alpha_x \alpha_y}}. \quad (\text{A10})$$

603 From the symmetricity to the plane $z = 0$, we can obtain,

$$604 \quad \hat{\varphi}(u, v) = -D \sqrt{1 - \left(\frac{u}{D}\right)^2 - \left(\frac{v}{D}\right)^2}, \quad (u, v) \in \hat{B}. \quad (\text{A11})$$

605 Inverse scaling coordinate transformation yields the ellipsoid phase boundary function as
 606 follows:

$$607 \quad \varphi(x, y) = -D \sqrt{1 - \left(\frac{x}{\alpha_x D}\right)^2 - \left(\frac{y}{\alpha_y D}\right)^2}, \quad (x, y) \in B, \quad (\text{A12})$$



608 where D is the depth of the talik at the center. The ellipsoid, the three-dimensional Stefan
609 Equation for talik, can be obtained by the isoperimetric inequality as well as the functional
610 analysis.

611 **Appendix B: Determination of the coefficients d and λ**

612 We can determine two coefficients in the ellipsoid (Equation 21) by further application of the
613 variational principle. Let

$$614 \quad D = \frac{2}{|\lambda|}. \quad (\text{B1})$$

615 Also, let the intersect d proportional to the vertical radius of the ellipsoid, as follows:

$$616 \quad d = tD \quad (-1 \leq t < 1), \quad (\text{B2})$$

617 where t is a parameter describing the relative elevation of the basin to the original ground surface.

618 Then, Equations (20) and (21) can be rewritten as,

$$619 \quad z = -\varphi = -\sqrt{D^2 - \frac{x^2}{\alpha_x^2} - \frac{y^2}{\alpha_y^2}} + tD, \text{ and} \quad (\text{B3})$$

$$620 \quad \left(\frac{x}{\alpha_x D}\right)^2 + \left(\frac{y}{\alpha_y D}\right)^2 + \left(\frac{z-tD}{D}\right)^2 = 1, \text{ respectively.} \quad (\text{B4})$$

621 Now, the phase boundary area and volume can be evaluated as functions of the parameter t :

$$\begin{aligned} 622 \quad V[\varphi] &= \iint_B \varphi \, dx dy = \iint_B \left(-\sqrt{D^2 - \frac{x^2}{\alpha_x^2} - \frac{y^2}{\alpha_y^2}} + tD\right) \, dx dy \\ &= \pi \alpha_x \alpha_y \int_{-(1-t)D}^0 \{D^2 - (tD - z)^2\} dz \\ &= \frac{\pi}{3} \alpha_x \alpha_y D^3 (t^3 - 3t + 2) \end{aligned} \quad (\text{B5})$$



$$\begin{aligned} A[\varphi] &= \iint_B \sqrt{\alpha_x^2 \varphi_x^2 + \alpha_y^2 \varphi_y^2 + 1} \, dx dy \\ &= \iint_B \frac{1}{\sqrt{1 - \left(\frac{x}{\alpha_x D}\right)^2 - \left(\frac{y}{\alpha_y D}\right)^2}} \, dx dy \\ &= \pi \alpha_x \alpha_y D^2 \left\{ (1 - t^2) + \int_1^{\frac{1}{t}} \left(\frac{1}{z^2} - t^2 \right) dz \right\} \\ &= 2\pi \alpha_x \alpha_y D^2 (1 - t) \end{aligned} \quad (B6)$$

Eliminating D from these expressions yields,

$$A[\varphi]^3 = M \frac{(1-t)^3}{(t^3 - 3t + 2)^2} \quad (B7)$$

where M is a positive constant. Therefore, as

$$\frac{d}{dt} (A[\varphi]^3) = M \frac{3t}{(1-t)^2(t+2)^3} > 0 \quad (-1 \leq t < 1), \quad (B8)$$

the phase boundary area $A[\varphi]$ is the minimum at $t = 0$. Hence, $d = 0$ that corresponds to a semi-ellipsoid with depth D at the center.

Author contribution

Ohara and Yamatani developed the theory, and all other co-authors, especially Hinkel, Jones, Parsekian, and Kanevskiy, offered crucial advice in interpretation. Jones and Parsekian provided the field observed data for the case study of Peatball Lake. Jones performed the statistical analysis on the oriented lakes based on SAR-satellite remote-sensing data. Ohara prepared the manuscript with contributions from all co-authors.

Acknowledgements

This study was supported by the National Science Foundation (NSF) under awards OPP-1806287, 1806213, and 1806202. The authors thank UIC Science and CH2MHill Polar Field



639 Services (now Battelle Arctic Research Operations) for logistical field support. Datasets and
640 sources code for this research are available in these in-text data citation references. Louise
641 Farquharson and Benjamin Gaglioti provided helpful comments improving the manuscript.

642 **References**

643 Arp, C. D., Jones, B. M., Schmutz, J. A., Urban, F. E., & Jorgenson, M. T.: Two mechanisms of
644 aquatic and terrestrial habitat change along an Alaskan Arctic coastline, *Polar Biology*,
645 33(12), 1629-1640, 2010.

646 Arp, C. D., Jones, B. M., Urban, F. E., & Grosse, G.: Hydrogeomorphic processes of thermokarst
647 lakes with grounded - ice and floating - ice regimes on the Arctic coastal plain,
648 Alaska, *Hydrological Processes*, 25(15), 2422-2438, 2011.

649 Arp, C. D., Whitman, M. S., Jones, B. M., Kemnitz, R., Grosse, G., & Urban, F. E.: Drainage
650 network structure and hydrologic behavior of three lake-rich watersheds on the Arctic
651 Coastal Plain, Alaska. *Arctic, Antarctic, and Alpine Research*, 44(4), 385-398, 2012.

652 Arp, C. D., Jones, B. M., Liljedahl, A. K., Hinkel, K. M., & Welker, J. A.: Depth, ice thickness,
653 and ice - out timing cause divergent hydrologic responses among Arctic lakes. *Water*
654 *Resources Research*, 51(12), 9379-9401, 2015.

655 Arp, C. D., Jones, B. M., Grosse, G., Bondurant, A. C., Romanovsky, V. E., Hinkel, K. M., &
656 Parsekian, A. D.: Threshold sensitivity of shallow Arctic lakes and sublake permafrost to
657 changing winter climate, *Geophysical Research Letters*, 43(12), 6358-6365, 2016.

658 Ashton, A.D., Murray, A.B., Littlewood, R., Lewis, D.A. and Hong, P.: Fetch-limited self-
659 organization of elongate water bodies, *Geology*, 37(2), pp.187-190, 2009.



- 660 Black, R. F., & Barksdale, W. L.: Oriented lakes of northern Alaska, *The Journal of Geology*,
661 57(2), 105-118, 1949.
- 662 Brewer, M. C.: The thermal regime of an arctic lake, *Eos, Transactions American Geophysical*
663 *Union*, 39(2), 278-284, 1958.
- 664 Burn, C. R., & Smith, M. W.: Development of thermokarst lakes during the Holocene at sites
665 near Mayo, Yukon Territory, *Permafrost and Periglacial Processes*, 1(2), 161-175, 1990.
- 666 Burn, C.R.: Tundra lakes and permafrost, Richards Island, western Arctic coast, Canada,
667 *Canadian Journal of Earth Sciences*, 39(8), pp.1281-1298, 2002.
- 668 Carslaw, H. S., & Jaeger, J. C.: *Conduction of heat in solids*. Oxford: Clarendon Press, 1959.
- 669 Carson, C. E.: Radiocarbon dating of lacustrine strands in Arctic Alaska. *Arctic*, 12-26, 1968.
- 670 Carson, C. E., & Hussey, K. M.: The oriented lakes of Arctic Alaska, *The Journal of Geology*,
671 70(4), 417-439, 1962.
- 672 Carter, L. D.: A Pleistocene sand sea on the Alaskan Arctic coastal plain, *Science*, 211(4480),
673 381-383, 1981.
- 674 Courant, R., & Hilbert, D.: *Methods of mathematical physics, Bulletin of the American*
675 *Mathematical Society*, 60, 578-579, 1954.
- 676 Creighton, A. L., Parsekian, A. D., Angelopoulos, M., Jones, B. M., Bondurant, A., Engram,
677 M., ... & Arp, C. D.: Transient electromagnetic surveys for the determination of talik
678 depth and geometry beneath thermokarst lakes, *Journal of Geophysical Research: Solid*
679 *Earth*, 123(11), 9310-9323, 2018.



- 680 DeWalle, D. R., & Rango, A.: Principles of snow hydrology, Cambridge University Press, 2008.
- 681 Doolittle, J. A., Hardisky, M. A., & Gross, M. F.: A ground-penetrating radar study of active
682 layer thicknesses in areas of moist sedge and wet sedge tundra near Bethel, Alaska, USA.
683 Arctic and Alpine Research, 22(2), 175-182, 1990.
- 684 Engram, M., Arp, C. D., Jones, B. M., Ajadi, O. A., & Meyer, F. J.: Analyzing floating and
685 bedfast lake ice regimes across Arctic Alaska using 25 years of space-borne SAR
686 imagery. Remote sensing of environment, 209, 660-676, 2018.
- 687 French, H. M.: The Periglacial Environment, Longman, New York, 1996.
- 688 Farquharson, L., Anthony, K.W., Bigelow, N., Edwards, M. and Grosse, G.: Facies analysis of
689 yedoma thermokarst lakes on the northern Seward Peninsula, Alaska. Sedimentary
690 Geology, 340, pp.25-37, 2016.
- 691 Gelfand, I. M., & Fomin, S. V.: Calculus of variations. Revised English edition translated and
692 edited by Richard A. Silverman. *Prentice Hall, Englewood Cliffs, NJ*, 7, 10-11, 1963.
- 693 Grosse, G., Jones, B. M., & Arp, C. D.: Thermokarst lakes, drainage, and drained basins. In:
694 Shroder, J. (Editor in Chief), Giardino, R., Harbor, J. (Eds.), *Treatise on Geomorphology*.
695 Academic Press, San Diego, CA, vol. 8, Glacial and Periglacial Geomorphology, pp.
696 325–353, 2013.
- 697 Heslop, J.K., Walter Anthony, K.M., Sepulveda-Jauregui, A., Martinez-Cruz, K., Bondurant, A.,
698 Grosse, G. and Jones, M.C.: Thermokarst lake methanogenesis along a complete talik
699 profile, Biogeosciences, 12(14), pp.4317-4331, 2015.



- 700 Hinkel, K. M., Frohn, R. C., Nelson, F. E., Eisner, W. R., & Beck, R. A.: Morphometric and
701 spatial analysis of thaw lakes and drained thaw lake basins in the western Arctic Coastal
702 Plain, Alaska, *Permafrost and Periglacial Processes*, 16(4), 327-341, 2005.
- 703 Hinkel, K. M., Sheng, Y., Lenters, J. D., Lyons, E. A., Beck, R. A., Eisner, W. R., & Wang, J.:
704 Thermokarst lakes on the Arctic coastal plain of Alaska: geomorphic controls on
705 bathymetry, *Permafrost and Periglacial Processes*, 23(3), 218-230, 2012.
- 706 Hinkel, K. M., & Arp, C.: Estimating talik depth beneath lakes in Arctic Alaska, In Proceedings,
707 7th Canadian Permafrost Conference and 68th Canadian Geotechnical Conference, pp.
708 20-23, 2015.
- 709 Hopkins, D. M.: Thaw lakes and thaw sinks in the Imuruk Lake area, Seward Peninsula, Alaska,
710 *The Journal of Geology*, 57(2), 119-131, 1949.
- 711 Hopkins, D. M., Karlstrom, T., Black, R., Williams, J., Pewe, T., Fernold, A., & Muller, E.:
712 Permafrost and ground water in Alaska, a shorter contribution to the general geology. US
713 Geol. Surv. Prof. Pap, 264, 1955.
- 714 Hunter, J. A., MacAulay, H. A., Gagné, R. M., Burns, R. A., Harrison, T. E., & Hawkins, J. P.:
715 Drained lake experiment for investigation of growth of permafrost at Illisarvik,
716 Northwest Territories—initial geophysical results, *Current research, part C. Geological*
717 *Survey of Canada, Paper*, 67-76, 1981.
- 718 Jeffries, M. O., Morris, K., Maksym, T., Kozlenko, N., & Tin, T.: Autumn sea ice thickness,
719 ridging and heat flux variability in and adjacent to Terra Nova Bay, Ross Sea, Antarctica,
720 *Journal of Geophysical Research: Oceans*, 106(C3), 4437-4448, 2001.



- 721 Johnston, G. H., & Brown, R. J. E.: Occurrence of permafrost at an Arctic lake, *Nature*,
722 211(5052), 952-953, 1966.
- 723 Jones, B. M., Grosse, G. D. A. C., Arp, C. D., Jones, M. C., Anthony, K. W., & Romanovsky, V.
724 E.: Modern thermokarst lake dynamics in the continuous permafrost zone, northern
725 Seward Peninsula, Alaska, *Journal of Geophysical Research: Biogeosciences*, 116(G2),
726 2011.
- 727 Jorgenson, M. T., & Shur, Y.: Evolution of lakes and basins in northern Alaska and discussion of
728 the thaw lake cycle, *Journal of Geophysical Research: Earth Surface*, 112(F2), 2007.
- 729 Kanevskiy, M., Shur, Y., Fortier, D., Jorgenson, M. T., & Stephani, E.: Cryostratigraphy of late
730 Pleistocene syngenetic permafrost (yedoma) in northern Alaska, Itkillik River exposure.
731 *Quaternary research*, 75(3), 584-596, 2011.
- 732 Kanevskiy, M., Shur, Y., Jorgenson, M. T., Ping, C. L., Michaelson, G. J., Fortier, D., ... &
733 Tumskoy, V.: Ground ice in the upper permafrost of the Beaufort Sea coast of Alaska,
734 *Cold Regions Science and Technology*, 85, 56-70, 2013.
- 735 Kanevskiy, M., Shur, Y., Strauss, J., Jorgenson, T., Fortier, D., Stephani, E., & Vasiliev, A.:
736 Patterns and rates of riverbank erosion involving ice-rich permafrost (yedoma) in
737 northern Alaska, *Geomorphology*, 253, 370-384, 2016.
- 738 Kessler, M. A., Plug, L. J., & Anthony, K. W.: Simulating the decadal - to millennial - scale
739 dynamics of morphology and sequestered carbon mobilization of two thermokarst lakes
740 in NW Alaska, *Journal of Geophysical Research: Biogeosciences*, 117(G2), 2012.



- 741 Kurylyk, B. L., & Hayashi, M.: Improved Stefan equation correction factors to accommodate
742 sensible heat storage during soil freezing or thawing. *Permafrost and Periglacial*
743 *Processes*, 27(2), 189-203, 2016.
- 744 Lachenbruch, A.H., Brewer, M.C., Greene, G.W., Marshall, B.V.: Temperatures in permafrost,
745 In *Temperature—Its Measurement and Control in Science and Industry*, 3, Herzfeld CM
746 (ed). Reinhold Publishing: New York; 791–803, 1962.
- 747 Lenz J, Jones BM, Wetterich S, Tjallingii R, Fritz M, Arp CD, Rudaya N, Grosse G. Impacts of
748 shore expansion and catchment characteristics on lacustrine thermokarst records in
749 permafrost lowlands, Alaska Arctic Coastal Plain. *arktos*. 2016 Dec;2(1):1-5., 2016.
- 750 Ling, F., & Zhang, T.: Impact of the timing and duration of seasonal snow cover on the active
751 layer and permafrost in the Alaskan Arctic, *Permafrost and Periglacial Processes*, 14(2),
752 141-150, 2003a.
- 753 Ling, F., and T. Zhang: Numerical simulation of permafrost thermal regime and talik
754 development under shallow thaw lakes on the Alaskan Arctic Coastal Plain, *J. Geophys.*
755 *Res.*, 108(D16), 4511, doi:10.1029/2002JD003014, 2003b.
- 756 Livingstone, D.A.: On the orientation of lake basins, *American Journal of Science*, 252: 547–554,
757 1954.
- 758 Lunardini, V.J.: *Heat Transfer in Cold Climates*, Van Nostrand Reinhold Co.: New York, NY;
759 731, 1981.
- 760 Mackay J.R.: *The Mackenzie Delta area, N.W.T. Geographical Branch Memoir 8*, Department of
761 *Mines and Technical Surveys*, Ottawa, 1963.



- 762 Mackay, J.R.: Lake stability in an ice-rich permafrost environment: examples from the western
763 Arctic coast. In: Robarts, R.D., Bothwell, M.L. (Eds.), *Aquatic Ecosystems in Semi-Arid*
764 *Regions: Implications for Resource Management*. NHRI Symposium Series 7.
765 Environment Canada, Saskatoon, Saskatchewan, pp. 1–26, 1992.
- 766 Ohara N., and Yamatani K.: Theoretical Stable Hydraulic Section based on the Principle of Least
767 Action. *Scientific Reports*, 9, Article number: 7957, 2019.
- 768 O’Neill, H. B., Roy - Leveillee, P., Lebedeva, L., & Ling, F.: Recent advances (2010-2019) in
769 the study of taliks, *Permafrost and Periglacial Processes*, 31(3), 346-357, 2020.
- 770 Parsekian, A. D., Creighton, A. L., Jones, B. M., & Arp, C. D.: Surface nuclear magnetic
771 resonance observations of permafrost thaw below floating, bedfast, and transitional ice
772 lakes, *Geophysics*, 84(3), EN33-EN45, 2019.
- 773 Painter, S. L., Coon, E. T., Atchley, A. L., Berndt, M., Garimella, R., Moulton, J. D., ... &
774 Wilson, C. J.: Integrated surface/subsurface permafrost thermal hydrology: Model
775 formulation and proof - of - concept simulations, *Water Resources Research*, 52(8),
776 6062-6077, 2016.
- 777 Patel, P. D.: Interface conditions in heat-conduction problems with change of phase, *AIAA*
778 *Journal*, 6(12), 2454-2454, 1968.
- 779 Pilon, J. A., Annan, A. P., & Davis, J. L.: Monitoring permafrost ground conditions with ground
780 probing radar (GPR), In *Workshop on Permafrost Geophysics*, Golden, Colorado. US
781 Army Corps of Engineers, Cold Regions Research and Engineering Laboratory, Hanover,
782 New Hampshire, CRREL Special Report (pp. 85-5), 1985.



- 783 Plug, L. J., & West, J. J.: Thaw lake expansion in a two - dimensional coupled model of heat
784 transfer, thaw subsidence, and mass movement, *Journal of Geophysical Research: Earth*
785 *Surface*, 114(F1), 2009.
- 786 Rampton, V. N.: Quaternary geology of the Yukon coastal plain, 1982.
- 787 Rangel R.C., A. D. Parsekian, L. M. Farquharson, B. M. Jones, N. Ohara, A. L. Creighton, B. V.
788 Gaglioti, M. Kanevskiy, A. L. Breen, H. Bergstedt, V. E. Romanovsky, and K. M.
789 Hinkel.: Geophysical Observations of Taliks Below Drained Lake Basins on the Arctic
790 Coastal Plain of Alaska. *Journal of Geophysical Research: Solid Earth* 126,
791 e2020JB020889. <https://doi.org/10.1029/2020JB020889>, 2020.
- 792 Reeve, D., Chadwick, A., & Fleming, C.: Coastal engineering: processes, theory and design
793 practice, CRC Press, 2018.
- 794 Rex, R. W.: Hydrodynamic analysis of circulation and orientation of lakes in Northern Alaska. In
795 *Geology of the Arctic*, Rauch GO (ed). University of Toronto Press: Toronto; 1021–1043,
796 1961.
- 797 Roy-Leveillee, P., & Burn, C. R.: Near - shore talik development beneath shallow water in
798 expanding thermokarst lakes, Old Crow Flats, Yukon, *Journal of Geophysical Research:*
799 *Earth Surface*, 122(5), 1070-1089, 2017.
- 800 Rowland, J. C., B. J. Travis, and C. J. Wilson: The role of advective heat transport in talik
801 development beneath lakes and ponds in discontinuous permafrost, *Geophys. Res. Lett.*,
802 38, L17504, doi:10.1029/2011GL048497, 2011.



- 803 Schuur, E. A., McGuire, A. D., Schädel, C., Grosse, G., Harden, J. W., Hayes, D. J., ... & Natali,
804 S. M.: Climate change and the permafrost carbon feedback. *Nature*, 520(7546), 171-179,
805 2015.
- 806 Sellmann, P. V.: *The classification and geomorphic implications of thaw lakes on the Arctic*
807 *Coastal Plain, Alaska* (Vol. 344), US Department of Defense, Department of the Army,
808 Corps of Engineers, Cold Regions Research and Engineering Laboratory, Report. 21 pp,
809 1975.
- 810 Séjourné, A., Costard, F., Fedorov, A., Gargani, J., Skorve, J., Massé, M., & Mège, D.:
811 Evolution of the banks of thermokarst lakes in Central Yakutia (Central Siberia) due to
812 retrogressive thaw slump activity controlled by insolation. *Geomorphology*, 241, 31-40,
813 2015.
- 814 Silvester, R., & Hsu, J. R.: *Coastal Stabilization*, Advanced Series on Ocean Engineering, Vol.
815 14, 1997.
- 816 Stefan J.: Über die Theorie der Eisbildung, insbesondere über die Eisbildung im Polarmee.
817 *Annals of Physics and Chemistry* 42: 269–286, 1891.
- 818 Schwamborn, G., Andreev, A., Rachold, V., Hubberten, H. W., Grigoriev, M. N., Tumskey,
819 V., ... & Dorozkhina, M. V.: Evolution of Lake Nikolay, Arga Island, Western Lena
820 River delta, during late pleistocene and holocene time, *Polarforschung*, 70, 69-82, 2000.
- 821 Sullivan, T. D., Parsekian, A. D., Sharp, J., Hanke, P. J., Thalasso, F., Shapley, M., ... & Walter
822 Anthony, K.: Influence of permafrost thaw on an extreme geologic methane seep.
823 *Permafrost and Periglacial Processes*, 2021.



- 824 Tomirdiaro, S. V.: Evolution of lowland landscapes in northeastern Asia during late Quaternary
825 time, In *Paleoecology of Beringia* (pp. 29-37). Academic Press, 1982.
- 826 West, J. J., and L. J. Plug: Time-dependent morphology of thaw lakes and taliks in deep and
827 shallow ground ice, *J. Geophys. Res.*, 113, F01009, doi:10.1029/2006JF000696, 2008.
- 828 Westermann, S., Schuler, T. V., Gislås, K., & Etzelmüller, B.: Transient thermal modeling of
829 permafrost conditions in Southern Norway, *The Cryosphere*, 7(2), 719-739, 2013.
- 830 van Everdingen, R.O. (Ed.): *Multi-Language Glossary of Permafrost and Related Ground-ice*
831 *Terms*, International Permafrost Association, The Arctic Institute of North America,
832 University of Calgary, Calgary, 268 pp, 1998.

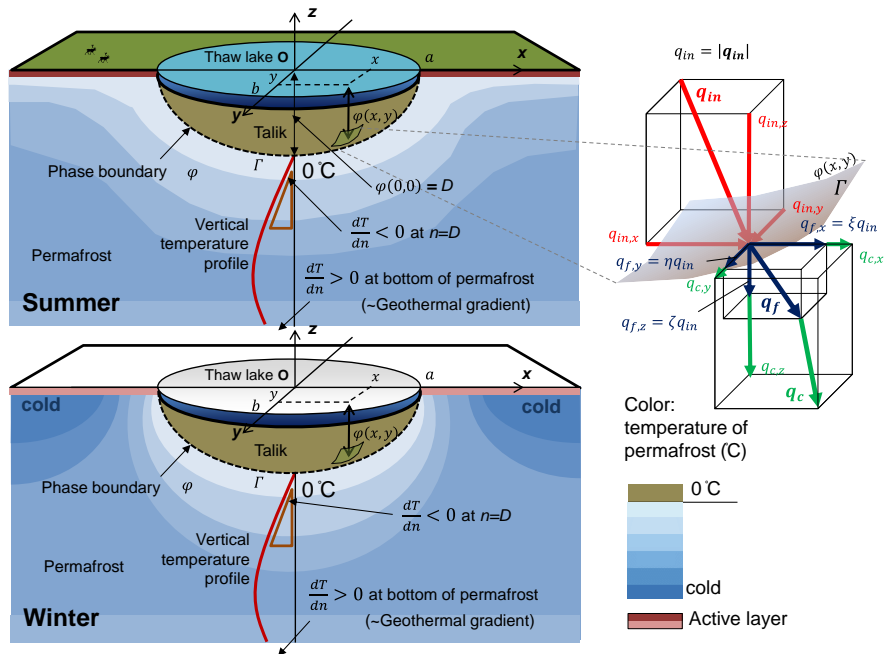


833 Table 1: Computed incoming heat flux with the estimated parameters

Parameter	Estimates	Unit	Note
Porosity	0.18		Sandstone >15 m deep; Creighton et al., 2018
Thermal conductivity of permafrost	2.20	W/(m·K)	From porosity and typical thermal properties of ice and mineral in this region
Talik depth, D	88.0	m	Fitted ellipsoid
Talik width (radius), a	514.8	m	Fitted ellipsoid
Aspect ratio, D/a	0.1709		Fitted ellipsoid
Geothermal gradient	0.0250	K/m	Kessler et al., 2012
dT/dz at the talik bottom	-0.0259	K/m	From Mackay model (1962)
Basin average heat flux, q_{in}	0.0689	W/m ²	Computed from Equation (29)

834

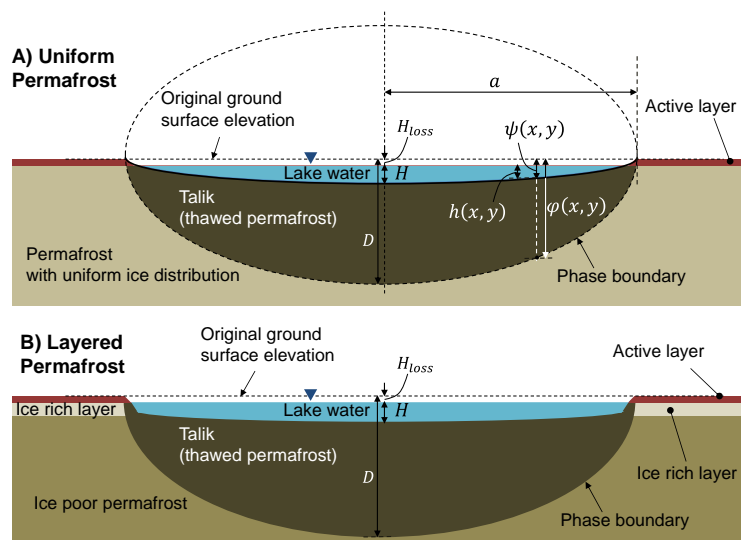
835



836

837 Figure 1: Definitions of variables associating with the overall shape of phase boundary φ during warm
 838 (Upper left panel) and cold seasons (Lower left panel) and incoming and outgoing heat transfers on
 839 $\varphi(x, y)$ (Right panel). Incoming heat (red colored vector) is perpendicular to the phase boundary
 840 $\varphi(x, y)$ while thaw direction (blue colored vector) is modified by the anisotropic heat conduction (green
 841 colored vector) in the permafrost.

842



843

844 Figure 2: Lake bathymetry models for a thermokarst lake and the talik underneath based on the quasi-
845 steady state. (A) The lake bathymetry is proportional to the talik geometry with uniform ice distribution.
846 (B) However, the lake bathymetry tends to have a flat bottom due to the widespread ice-rich layer near
847 the surface.

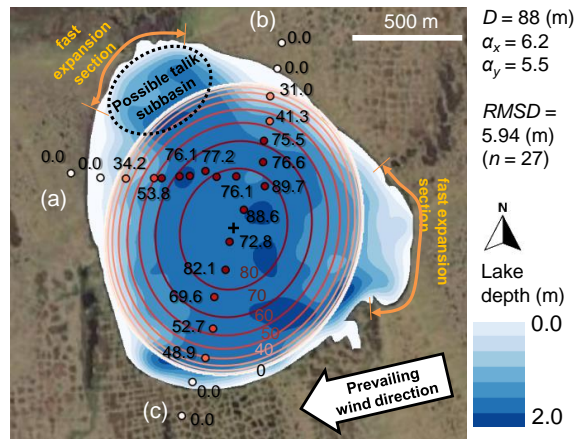
848



849

850 Figure 3: Map of the study area: Peatball Lake and subregions for lake characterization (red).

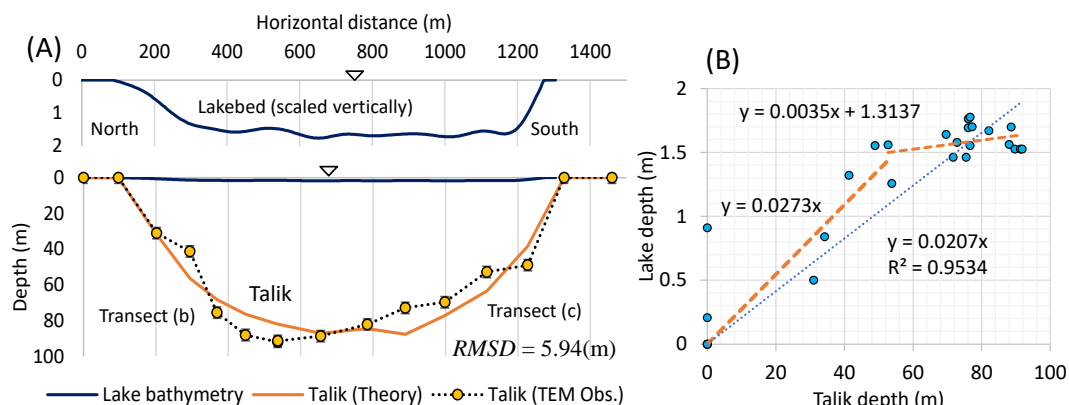
851



852

853 Figure 4: The theoretically extrapolated talik thickness map (contour lines) based on 27 TEM soundings
854 (dots) in Peatball Lake, ACP of Alaska. The red contour lines and the observation points are consistent.
855 The corresponding observed lake bathymetry (adopted from Lenz et al., 2016) is also included in blue
856 gradation. The TEM sounding transects start on the lakeshore and end near the center of the lake.

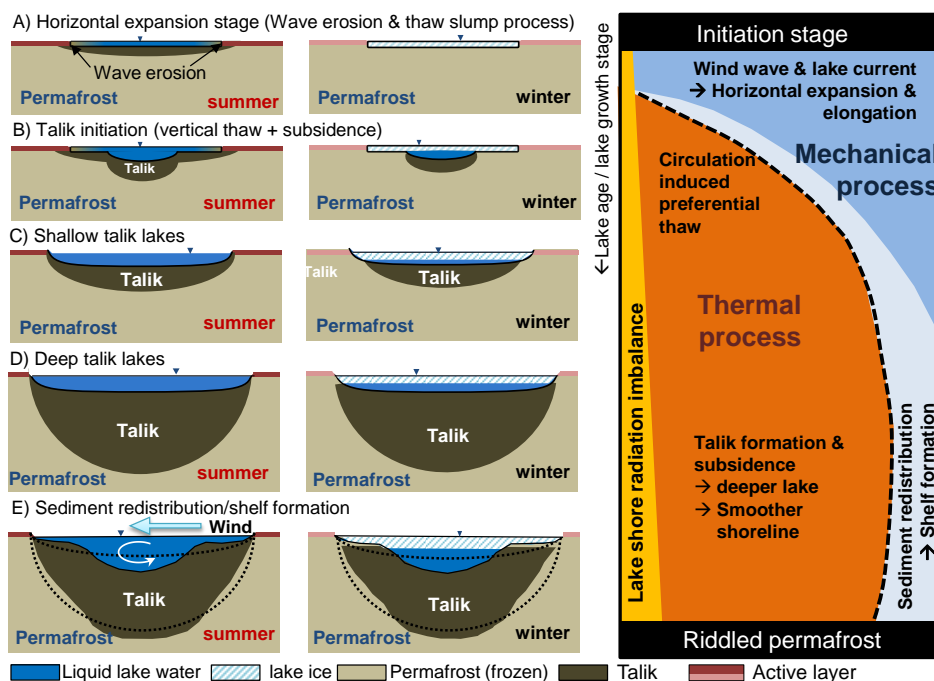
857



858

859 Figure 5: Cross sectional comparisons of the lakebed and the talik profiles along two TEM transects (b)
860 through (c) (Lenz et al., 2016) in Peatball Lake. Panel (B) displays the cross plot of the observed talik
861 and lake depths at all 27 TEM data points.

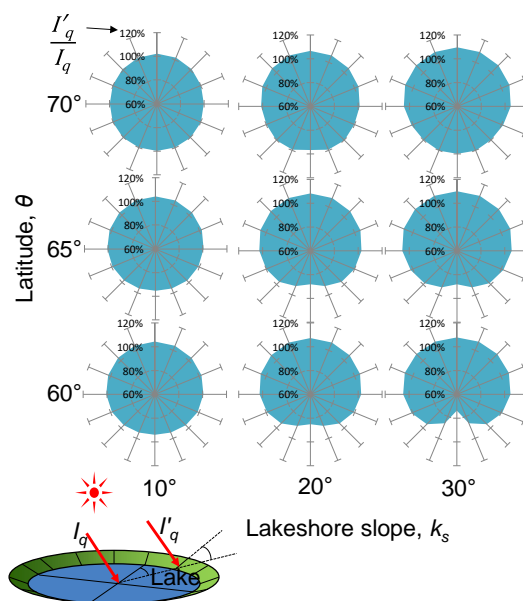
862



863

864 Figure 6: Combined hypothetical models of thermokarst lake evolution and diagram of major influencing
 865 factors through time. The left column represents summer conditions, the center column represents winter
 866 conditions, and the right column indicates the corresponding importance of mechanical vs. thermal
 867 processes through time as the lake ages (top is younger, bottom is older). Row (A) indicates the early
 868 processes under bedfast ice conditions before talik initiation. Row (B) shows the onset of vertical thaw
 869 and subsidence as talik begins to develop. Row (C) shows early, shallow talik growth conditions. Row
 870 (D) indicates later stage processes on deepened talik due to vertical thaw. Row (E) is the mature stage of
 871 development when complex bathymetry has set in as a result of sediment transport.

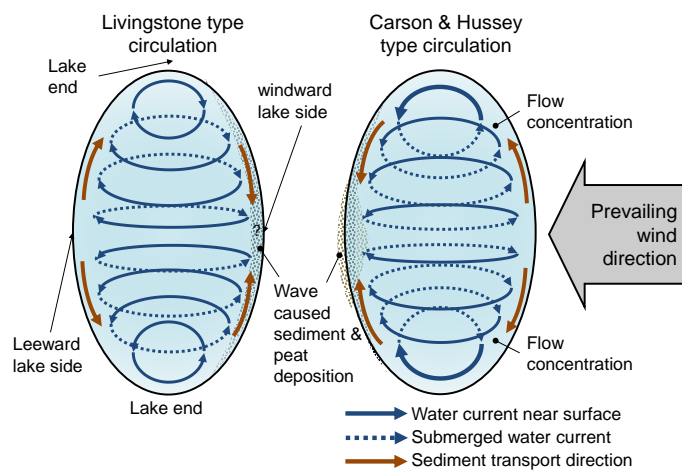
872



873

874 Figure 7: Computed mean daily potential solar radiation on sloping lakeshore relative to the flat surface
875 during summer period (June-August) with respect to latitude. I_q is the potential solar radiation on a flat
876 surface, and I'_q is radiation on sloping lakeshore.

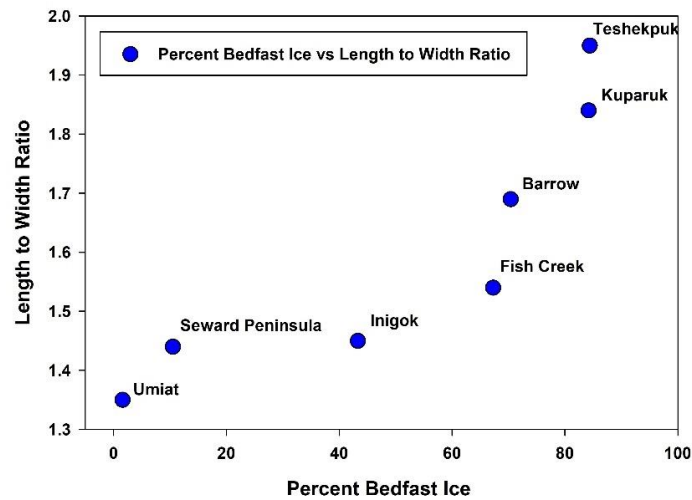
877



878

879 Figure 8: Two distinctive lake water circulation patterns created by unidirectional wind. Livingstone type
880 circulation and Carson & Hussey type circulation causes opposite flow directions around lake ends. This
881 also results in difference in sediment and peat deposition patterns.

882



883

884 Figure 9: Comparison of Length to Width ratio versus the percent of a particular region exhibiting a
885 bedfast lake ice regime for seven study areas in Arctic Alaska. This analysis is based on SAR-satellite
886 remote-sensing data presented in Ingram et al., 2018. Lakes that are more elliptical in shape tend to
887 occur where the majority of the lakes in the area freeze to their bed and thus likely do not have a talik.
888 Lakes that are more circular in shape tend to occur where the majority of lakes in an area do not freeze to
889 their bed and thus likely have a sub-lake talik.

890